



## Facile preparation of a $\text{Na}_2\text{MnSiO}_4/\text{C}/\text{graphene}$ composite as a high performance cathode for sodium ion batteries<sup>†</sup>

Hai Zhu, Juntao Wang, Xiaoling Liu and Xiaoming Zhu\*

A new class of  $\text{Na}_2\text{MnSiO}_4/\text{carbon}/\text{graphene}$  ( $\text{Na}_2\text{MnSiO}_4/\text{C}/\text{G}$ ) composite is successfully prepared and investigated for use as a cathode material for Na ion batteries. X-ray diffraction confirms that formation of a monoclinic structure with *Pn* space group. Morphological characterization shows that  $\text{Na}_2\text{MnSiO}_4$  nanoparticles, about 30–40 nm in size with high density, are homogeneously anchored on the whole surface of the crumpled micrometer-size graphene nanosheets. The sodium insertion–extraction process of  $\text{Na}_2\text{MnSiO}_4$  is similar to that of  $\text{Li}_2\text{MnSiO}_4$  as a cathode in Li ion batteries. Compared with the  $\text{Na}_2\text{MnSiO}_4/\text{C}$  composite, the  $\text{Na}_2\text{MnSiO}_4/\text{C}/\text{G}$  composite shows much better electrochemical performance, including excellent rate performance and capacity retention. At the rate of 0.1C (1C = 139 mA h g<sup>−1</sup>), the discharge capacity of the initial cycle is 182.4 mA h g<sup>−1</sup>, corresponding to 1.31 Na<sup>+</sup> insertion per  $\text{Na}_2\text{MnSiO}_4$  molecule. Even at high rates of 1C, 2C and 5C, the composite exhibits discharge capacities of 106.9, 80.3 and 60.7 mA h g<sup>−1</sup>, respectively. The enhanced electrochemical performance arises from the conductive graphene nanosheets, which facilitate the electronic conductivity of the composite, improve the contact area for the electrode/electrolyte interface and decrease the particles sizes of  $\text{Na}_2\text{MnSiO}_4$ , as well as can reduce the diffusion length of Na<sup>+</sup> ions.

Received 6th January 2017  
Accepted 25th February 2017

DOI: 10.1039/c7ra00198c  
[rsc.li/rsc-advances](http://rsc.li/rsc-advances)

### 1. Induction

Recently, in order to solve the problem of energy shortage and environmental pollution, rechargeable batteries for large-scale electrical storage applications have been developed rapidly.<sup>1,2</sup> With high power density, high energy conversion efficiency and long cycling life, lithium ion batteries have been widely considered to be one of the most promising electrochemical secondary battery technologies.<sup>3,4</sup> However, there are still several significant challenges for its further development due to the shortage of the limited lithium resource and safety issues. In contrast to lithium ion batteries, sodium ion batteries have many advantages, such as more abundant resources, lower cost, better safety performance and sodium's physical and chemical properties are similar to those of Li.<sup>5–7</sup> Therefore, sodium ion batteries have gained increased recognition as a reasonable candidate to replace lithium ion batteries for energy conversion and storage systems.

So far, many sodium ion based materials have been investigated to develop desirable cathode materials for sodium ion

batteries. Among the compounds, most of the studies are focused on the layered compounds ( $\text{Na}_x\text{CoO}_2$ ,<sup>8,9</sup>  $\text{Na}_x\text{MnO}_2$ ,<sup>10,11</sup>  $\text{NaFeO}_2$ ,<sup>12</sup>  $\text{Na}_{2/3}\text{Co}_{2/3}\text{Mn}_{1/3}\text{O}_2$ ,<sup>13</sup>) and polyanionic compounds ( $\text{Na}_3\text{V}_2(\text{PO}_4)_3$ ,<sup>14,15</sup>  $\text{NaFePO}_4$ ,<sup>16</sup>  $\text{Na}_2\text{Fe}_2(\text{SO}_4)_3$  (ref. 17)). Although the layered compounds with unique layered structure is conducive to Na<sup>+</sup> insertion/extraction and these materials as Na ion storage materials with high capacities and voltage platform, their capacity retention capability is unsatisfactory. For instance, Morales *et al.*<sup>18</sup> showed the layered  $\text{P}_2\text{-Na}_{0.6}\text{MnO}_2$  with an initial discharge capacity of 150 mA h g<sup>−1</sup>, but its capacity retention is less than 50% after only 10 cycles. In general, polyanionic compounds exhibit better capacity retention and thermal stability than the layered transition metal oxides because of their structural diversity and stability. However, polyanion cathode materials are facing the problems of poor capacity and rate capability for large-scale grid applications.

More recently,  $\text{Na}_2\text{MSiO}_4$  (M = Fe, Mn) has also been identified as potential electroactive cathode material due to its high theoretical capacity (>270 mA h g<sup>−1</sup> is possible when extracting two Na<sup>+</sup> ions per molecule), low cost, high operating potential and structural robustness. However, as a promising cathode material for sodium ion batteries,  $\text{Na}_2\text{MSiO}_4$  also suffers from poor electrical conductivity due to the polyanion structure. To date, only a few reports have been published for electrochemical characterization of  $\text{Na}_2\text{MSiO}_4$  in sodium ion batteries. Zhang *et al.*<sup>19</sup> synthesized  $\text{Na}_2\text{FeSiO}_4$  from  $\text{Li}_2\text{FeSiO}_4$  undergo the electrochemical Li–Na ion exchange process, which could

R & D Center for Non-power Nuclear Technology, School of Nuclear Technology and Chemistry & Biology, Hubei University of Science and Technology, Xianning 437100, China. E-mail: [energy603@163.com](mailto:energy603@163.com)

† Electronic supplementary information (ESI) available: TEM images of  $\text{Na}_2\text{MnSiO}_4/\text{G}$  and  $\text{Na}_2\text{MnSiO}_4/\text{C}$ , TGA curves of  $\text{Na}_2\text{MnSiO}_4/\text{G}$  and  $\text{Na}_2\text{MnSiO}_4/\text{C}$ , and cycling performances of the  $\text{Na}_2\text{MnSiO}_4/\text{C}/\text{G}$  and the  $\text{Na}_2\text{MnSiO}_4/\text{C}$  composites at 0.1C. See DOI: [10.1039/c7ra00198c](https://doi.org/10.1039/c7ra00198c)



deliver a specific capacity as high as 330  $\text{mA h g}^{-1}$  in the Na cells at the current density of 10  $\text{mA g}^{-1}$  and at room temperature. Chen *et al.*<sup>20</sup> synthesized *Pn* phase  $\text{Na}_2\text{MnSiO}_4$  by a sol-gel method, and demonstrated the composite with discharge capacity of 125  $\text{mA h g}^{-1}$  for the battery operate at 13.9  $\text{mA g}^{-1}$  and 363 K. However, for  $\text{Na}_2\text{MnSiO}_4$ , there is still no scientific report in literature about the usage of graphene, and no reports of the  $\text{Na}^+$  ion migration dynamics on *Pn* phase  $\text{Na}_2\text{MnSiO}_4$  as cathode for sodium ion batteries.

In this study, we have synthesized  $\text{Na}_2\text{MnSiO}_4/\text{C}/\text{G}$  composite by a sol-gel method and the electrochemical characteristics of the composite were investigated. As a cathode material for sodium ion batteries, the  $\text{Na}_2\text{MnSiO}_4/\text{C}/\text{G}$  composite can deliver discharge capacities of above 180  $\text{mA h g}^{-1}$  at the rate of 0.1C (13.9  $\text{mA g}^{-1}$ ) at room temperature, and it has higher rate performance and better capacity retention compare with other products of  $\text{Na}_2\text{MnSiO}_4/\text{C}$  which were prepared without graphene nanosheets. The much improved electrochemical properties is ascribed to the good conductivity and high special surface area of graphene, which can prominently enhance the electronic conductivity of the cathode material. Moreover, the adding of graphene oxide in the synthesis process could decrease the particles sizes of  $\text{Na}_2\text{MnSiO}_4$  and prevent the aggregation of nanoparticles, the homogeneous dispersion and nanoscale size of particles can shorten the migration path of  $\text{Na}^+$  ion.

## 2. Experimental

### 2.1 Materials synthesis

The  $\text{Na}_2\text{MnSiO}_4/\text{C}/\text{G}$  composite was prepared though a facile sol-gel method and subsequent annealing. The graphene oxide (GO) nanosheets were obtained by a modified Hummers' method.<sup>21</sup> In a typical synthesis, 60 mg GO was firstly dispersing in 30 mL deionized water *via* ultrasonication, and then 1 g glucose, 4 mmol  $\text{CH}_3\text{COONa}$  and 2 mmol  $\text{Mn}(\text{CH}_3\text{COO})_2 \cdot 4\text{H}_2\text{O}$  were added, dissolved. Subsequently, the solution of 2 mmol tetraethyl orthosilicate (TEOS, CP) and 20 mL isopropanol was added into the previously mixed solution. Under continuous stirring, the pH was adjusted to a value lower than 4.0 by addition of acetic acid and the temperature of the solution was heated to 70 °C to evaporate the solvent. The resulting dry gel was ground with a mortar and then calcined in a furnace tube at 650 °C (at a rate of 2 °C min<sup>-1</sup>) for 10 h in flowing argon,  $\text{Na}_2\text{-MnSiO}_4/\text{C}/\text{G}$  composite was obtained. For comparison, the same synthesis procedure was used to prepared  $\text{Na}_2\text{MnSiO}_4/\text{C}$  composite except that GO was not added and the amount of glucose was increased to 2 g.

### 2.2 Materials characterizations

The crystalline structures of the samples were characterized by the X-ray diffractometer (XRD, Bruker D8 Advance, Cu K $\alpha$  radiation,  $\lambda = 0.15418$  nm). The Raman spectra was carried out on a Renishaw 2000 model confocal Raman micro-spectroscope with 636 nm line of a He-Ne laser radiation in the range of 400–2000  $\text{cm}^{-1}$ . The morphologies and compositions of the samples were observed with a scanning electron microscopy (SEM,

SIRION, FEI, USA) and transmission electron microscopy (TEM, JEM-2001F, JEOL, operating at 200 kV). Elemental analyzer (Elementar Analysen System GmbH, Germany) were conducted to measure the value of the carbon contents in the composites. The carbon contents of  $\text{Na}_2\text{MnSiO}_4/\text{C}/\text{G}$  and  $\text{Na}_2\text{MnSiO}_4/\text{C}$  composites are 23.1% and 22.9%, respectively. Thermal gravimetric analysis (TGA) experiment was performed on a Netzsch STA409 (heating rate = 10 °C min<sup>-1</sup>, 30 to 1000 °C, air flow).

### 2.3 Electrochemical measurements

The electrochemical properties of Na-based electrode materials were carried out using a coin type cell (CR2016) at room temperature. The working electrodes were fabricated by mixing the 75 wt% of active materials, 20 wt% of acetylene black and 5 wt% of polyvinylidene fluoride (PVDF) binder and then spread onto stainless steel meshes that were used as the current collectors and dried at 60 °C for 12 h. Na metal foil was used as the counter electrode. The electrolyte was based on 1 M  $\text{NaClO}_4$  dissolved in a mixture of propylene carbonate (PC) and fluoro ethylene carbonate (FEC) (1 : 1 by volume) solvents. The Celgard 2500 microporous film was used as separator. The cells were assembled in a glove box filled with high purity argon gas. Galvanostatic charge and discharge measurements were tested at different current densities on a battery test system (Neware, Shenzhen, China) in the voltage window of 1.5–4.2 V (vs.  $\text{Na}^+/\text{Na}$ ) at room temperature. All the charge-discharge specific capacities mentioned in this paper were calculated on the net weight of  $\text{Na}_2\text{MnSiO}_4$  by excluding other materials contents. Electrochemical impedance spectroscopy (EIS) were conducted using an electrochemistry workstation (CHI 660C) by applying an alternating-current signal amplitude of 10 mV in the frequency range from 100 kHz to 0.1 Hz.

## 3. Results and discussion

The crystal structures and phase composition of the as-prepared samples were examined by the XRD pattern, as shown in Fig. 1. As can be seen, the same characteristic peaks in the curves of  $\text{Na}_2\text{MnSiO}_4/\text{C}/\text{G}$  and  $\text{Na}_2\text{MnSiO}_4/\text{C}$  composites can be perfectly assigned to the monoclinic *Pn* structure of  $\text{Na}_2\text{MnSiO}_4$  (JCPDS No. 55-0638), which is consistent with that obtained by Duncan *et al.*<sup>22</sup> (S.G. *Pn*,  $a = 6.9637$  Å,  $b = 5.6101$  Å,  $c = 5.2988$  Å, and  $\beta = 89.780^\circ$ ). In addition, a minor impurity phase of manganese oxides can be found in the as-prepared composites. Compared with the XRD pattern of  $\text{Na}_2\text{MnSiO}_4/\text{C}$ , the diffraction peaks of the  $\text{Na}_2\text{MnSiO}_4/\text{C}/\text{G}$  composite appeared much weaker and broader, indicating that the  $\text{Na}_2\text{MnSiO}_4$  crystals in the  $\text{Na}_2\text{-MnSiO}_4/\text{C}/\text{G}$  is smaller than the crystals in the  $\text{Na}_2\text{MnSiO}_4/\text{C}$  due to the existence of graphene. Calculations using Scherrer formula ( $D = k\lambda/(B \cos \theta)$ , where  $k$  is 0.89) revealed the average grain sizes are ~40 and ~150 nm for the  $\text{Na}_2\text{MnSiO}_4/\text{C}/\text{G}$  and  $\text{Na}_2\text{MnSiO}_4/\text{C}$  composites, respectively. In addition, no peaks of graphene are detected in the XRD pattern of  $\text{Na}_2\text{MnSiO}_4/\text{C}/\text{G}$  owing to the  $\text{Na}_2\text{MnSiO}_4$  at  $2\theta \approx 26^\circ$  will also appear an diffraction peak, which overlap with the diffraction peak of graphene.



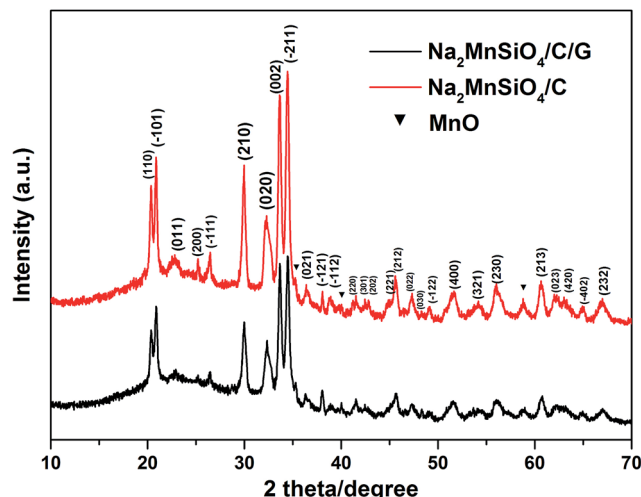


Fig. 1 The XRD patterns of the  $\text{Na}_2\text{MnSiO}_4/\text{C}/\text{G}$  and  $\text{Na}_2\text{MnSiO}_4/\text{C}$  composites.

Raman spectra was performed to further confirm the degree of crystallinity of the carbon in the composites.<sup>23</sup> The Raman spectrum of the  $\text{Na}_2\text{MnSiO}_4/\text{C}/\text{G}$  (Fig. 2) gives two bands and can be further deconvoluted into four Gaussian bands at 1604, 1532, 1350, 1261  $\text{cm}^{-1}$ , which further evaluate the presence of graphene and carbon layer. The two characteristic peaks are observed at around 1350 and 1604  $\text{cm}^{-1}$  corresponding to the characteristic D and G bands of carbons, respectively. The D band is assigned to defects and disordered portions of  $\text{sp}^3$  carbon, and the G band is indicated to the ordered  $\text{sp}^2$  carbon network in the composites. The peak intensity ratio between the D and G bands ( $I_{\text{D}}/I_{\text{G}}$ ) can be used to evaluate the degree of ordering in carbon materials, with a lower ratio of  $I_{\text{D}}/I_{\text{G}}$  corresponding to a higher degree of ordering.<sup>24</sup> The  $I_{\text{D}}/I_{\text{G}}$  ratio for the  $\text{Na}_2\text{MnSiO}_4/\text{C}/\text{G}$  composite is found to be 0.84, demonstrating the existence of carbon coating layer and graphene in the  $\text{Na}_2\text{MnSiO}_4/\text{C}/\text{G}$  composite is fairly ordered.

Morphological features of the as-obtained samples were investigated and the SEM and TEM images are provided in

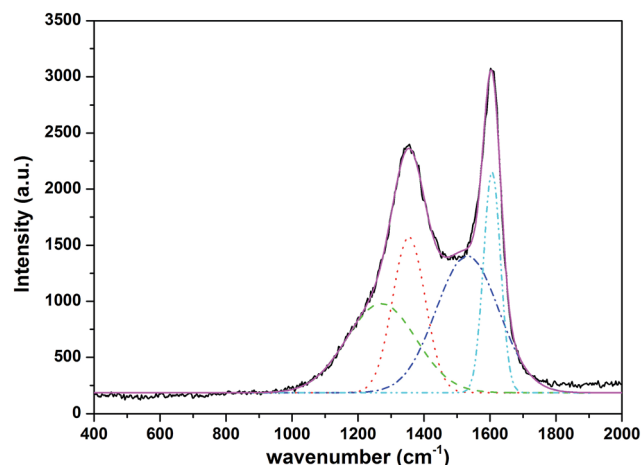


Fig. 2 The Raman spectrum of the  $\text{Na}_2\text{MnSiO}_4/\text{C}/\text{G}$  composite.

Fig. 3. The SEM image (Fig. 3a) of the obtained  $\text{Na}_2\text{MnSiO}_4/\text{C}/\text{G}$  composite reveals  $\text{Na}_2\text{MnSiO}_4$  nanoparticles are scattered on the surface of the graphene layer. Meanwhile, the TEM analysis (Fig. 3b) indicates that  $\text{Na}_2\text{MnSiO}_4$  nanoparticles of about 30–40 nm in size with high density, which are homogeneously anchored on the whole surface of the crumpled micrometer-size graphene sheets. In contrast, as seen in Fig. 3c and d, the  $\text{Na}_2\text{MnSiO}_4/\text{C}$  consists of irregular congregated particles with size of 100–200 nm, which is larger than that of  $\text{Na}_2\text{MnSiO}_4/\text{C}/\text{G}$  and is not well distributed. It is demonstrated that the adding of GO nanosheets into the synthesis precursor solution could decrease the particle size and inhibit the aggregation of the  $\text{Na}_2\text{MnSiO}_4$  crystal particles. This may be due to a lot of oxygen functional groups are located on the surfaces of GO nanosheets, providing electrostatic forces to adsorb positively charged ions and hinder the diffusion of small molecules. The oxygen-containing defect sites of graphene nanosheets limit the size and agglomeration of the  $\text{Na}_2\text{MnSiO}_4$  crystal particles during the crystallizing process.<sup>25</sup> As seen in Fig. S1a,† the particle size of  $\text{Na}_2\text{MnSiO}_4/\text{G}$  ( $\text{Na}_2\text{MnSiO}_4/\text{G}$  prepared with only GO) is about 45 nm, which is closed to the size of  $\text{Na}_2\text{MnSiO}_4/\text{G}$ . When the  $\text{Na}_2\text{MnSiO}_4/\text{C}$  prepared with the same amount of glucose to  $\text{Na}_2\text{MnSiO}_4/\text{C}/\text{G}$ , it can be seen from the TEM image in Fig. S1b† that the  $\text{Na}_2\text{MnSiO}_4/\text{C}$  particles with size in the range of 150–300 nm. The above results further confirming that the adding of GO nanosheets into the precursor solution could decrease the particle size.

The  $\text{Na}_2\text{MnSiO}_4/\text{C}/\text{G}$  composite is selected for further investigation by TEM and high resolution TEM (HRTEM). TEM image (Fig. 4a) at higher magnification clearly reveal that the  $\text{Na}_2\text{MnSiO}_4$  nanoparticles are confined in between the graphene nanosheets to form a sandwich structure. The HRTEM image (Fig. 4b) focused on an individual  $\text{Na}_2\text{MnSiO}_4$  nanoparticle anchored on graphene nanosheets. The regular lattice fringes of the nanoparticle can be clearly seen and the lattice spacing is measured to be 0.266 nm (the lower inset in Fig. 4b), corresponding to the interplanar distance of the (002) lattice plane of *Pn* phase  $\text{Na}_2\text{MnSiO}_4$ . This can also be validated according to the diffraction spots of  $\text{Na}_2\text{MnSiO}_4$  by the corresponding fast Fourier transform (FFT) image (the top inset in Fig. 4b). Meanwhile, both the graphene nanosheets and the thin carbon coating layer around the particle can be clearly observed, the layer-by-layer feature is obviously discernable. In this kind of structure, the double carbon layer may be beneficial to enhance the surface electronic conductivity of the composite. The carbon content in these samples was also determined *via* thermal gravimetric analysis (TGA), as shown in Fig. S2.† In theory, the thermal decomposition of the pure  $\text{Na}_2\text{MnSiO}_4$  will suffered from a weight increase from 100% to 103.3% in air, because of the decomposition of the material to produce  $\text{Na}_2\text{O}$ ,  $\text{Mn}_3\text{O}_4$  and  $\text{SiO}_2$ . According to the TGA results, the weight content of carbon in the  $\text{Na}_2\text{MnSiO}_4/\text{C}/\text{G}$  and  $\text{Na}_2\text{MnSiO}_4/\text{C}$  composites are calculated to be 24.9% and 23.4%, respectively.

The electrochemical properties of the as-prepared composites were evaluated in the sodium ion batteries configuration in the voltage range of 1.5–4.2 V (vs.  $\text{Na}^+/\text{Na}$ ) at room temperature. Fig. 5 compares the typical charge–discharge curves of the



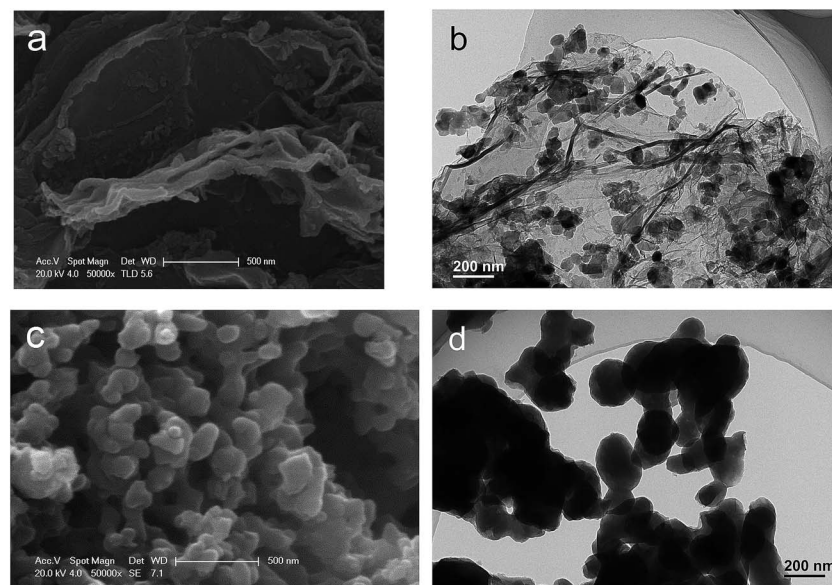


Fig. 3 Morphological features of the as-obtained samples: SEM (a) and TEM (b) images for  $\text{Na}_2\text{MnSiO}_4/\text{C}/\text{G}$  composite; SEM (c) and TEM (d) images for  $\text{Na}_2\text{MnSiO}_4/\text{C}$  composite.

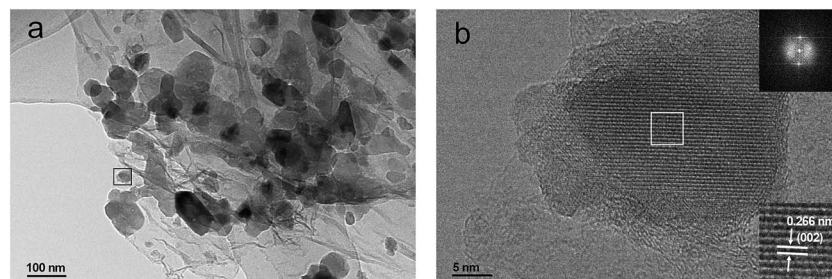


Fig. 4 The TEM (a) and high-resolution TEM (b) images of the  $\text{Na}_2\text{MnSiO}_4/\text{C}/\text{G}$  composite.

$\text{Na}_2\text{MnSiO}_4/\text{C}/\text{G}$  and  $\text{Na}_2\text{MnSiO}_4/\text{C}$  electrodes at a rate of 0.1C (1C = 139 mA h g<sup>-1</sup>) in the initial 5 cycles. As presented in Fig. 5a, the first charge curve of  $\text{Na}_2\text{MnSiO}_4/\text{C}/\text{G}$  with a long voltage plateau region around 3.2 V, and it has been slowly

rising up to 4.2 V, which can be ascribed to the initial oxidation of  $\text{Mn}^{2+}$  to  $\text{Mn}^{3+}$  and  $\text{Mn}^{4+}$ , and the irreversible decomposition of partial electrolyte.<sup>26,27</sup> Meanwhile, the first charge and discharge capacities are 260.8 and 182.4 mA h g<sup>-1</sup>, respectively,

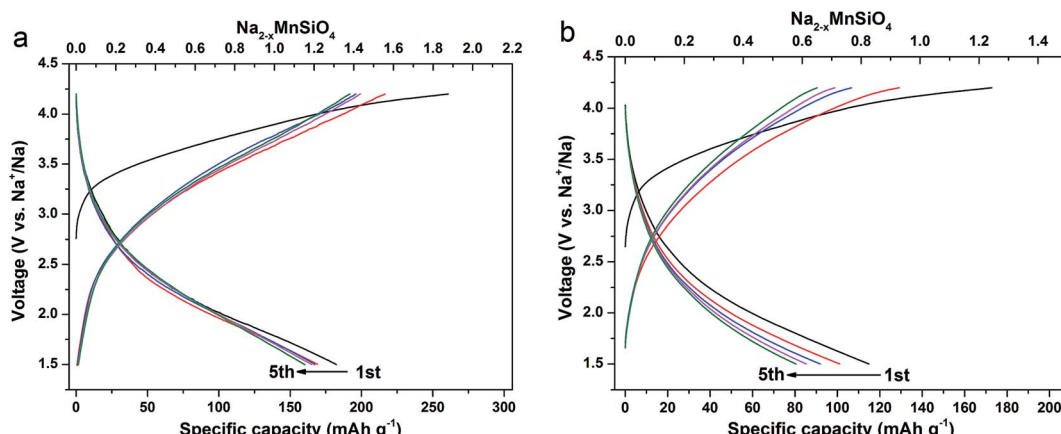


Fig. 5 The galvanostatic charge–discharge curves at the rate of 0.1C for the initial 5 cycles for the  $\text{Na}_2\text{MnSiO}_4/\text{C}/\text{G}$  (a) and  $\text{Na}_2\text{MnSiO}_4/\text{C}$  (b) composites.

with a coulombic efficiency of 70.04%. The irreversible capacity loss can be attributed to the formation of solid electrolyte interphase (SEI) layer, as well as the decomposition of electrolyte under the high voltage. Similar to  $\text{Li}_2\text{MnSiO}_4$ , the succeeding charge plateau of  $\text{Na}_2\text{MnSiO}_4$  was obviously lower than the initial one, which suggested that a structural rearrangement might occur during the initial charge process.<sup>28–30</sup> It is mentioning noting that the discharge capacities of  $\text{Na}_2\text{MnSiO}_4/\text{C}/\text{G}$  composite in initial 5 cycles are 182.4, 169.2, 167.3, 165.2 and 160.4  $\text{mA h g}^{-1}$ , corresponding to 1.31, 1.22, 1.20, 1.18 and 1.15  $\text{Na}^+$  insertion per  $\text{Na}_2\text{MnSiO}_4$  molecule, respectively. In the case of the  $\text{Na}_2\text{MnSiO}_4/\text{C}$  (Fig. 5b), although the trend of charge–discharge curves of  $\text{Na}_2\text{MnSiO}_4/\text{C}$  is similar to that of  $\text{Na}_2\text{MnSiO}_4/\text{C}/\text{G}$ , the discharge capacities of the  $\text{Na}_2\text{MnSiO}_4/\text{C}$  electrode is much lower than the counterparts in the case of the  $\text{Na}_2\text{MnSiO}_4/\text{C}/\text{G}$  electrode. For the  $\text{Na}_2\text{MnSiO}_4/\text{C}$  composite, the discharge capacities in initial 5 cycles are 114.9, 101.1, 91.9, 85.3 and 80.5  $\text{mA h g}^{-1}$ , respectively, which are 63.0%, 59.7%, 54.9%, 51.7% and 50.1%, respectively, of the discharge capacities in the same cycles for the  $\text{Na}_2\text{MnSiO}_4/\text{C}/\text{G}$  composite. The cycling performances of the  $\text{Na}_2\text{MnSiO}_4/\text{C}/\text{G}$  and the  $\text{Na}_2\text{MnSiO}_4/\text{C}$  composites at 0.1C are showed in Fig. S3.† As can be seen, after being charge–discharge 100 times, the capacity retention of the  $\text{Na}_2\text{MnSiO}_4/\text{C}/\text{G}$  composite can still maintain at 44.7% while it is only 23.6% for the  $\text{Na}_2\text{MnSiO}_4/\text{C}$  composite. Furthermore, for both composites, the discharge capacities decreased with the

increasing cycle times. We attribute the capacity decay in our product to the amorphization of  $\text{Na}_2\text{MnSiO}_4$  crystals in the composites during the  $\text{Na}^+$  ion insertion/extraction process.

To investigate the rate dependent cycling performances of the  $\text{Na}_2\text{MnSiO}_4/\text{C}/\text{G}$  and  $\text{Na}_2\text{MnSiO}_4/\text{C}$  composites, galvanostatic charge–discharge measurements were also curried out under various rates. Fig. 6 reveals the charge–discharge profiles of the two composites and the corresponding cycle stabilities at different rates for 30 cycles. Obviously, the  $\text{Na}_2\text{MnSiO}_4/\text{C}/\text{G}$  composite show higher discharge capacities and better cycle performance than  $\text{Na}_2\text{MnSiO}_4/\text{C}$  composite at each rate. For example, the initial discharge capacities of  $\text{Na}_2\text{MnSiO}_4/\text{C}/\text{G}$  (Fig. 6a and b) are 130.1, 106.9, 80.3 and 60.7  $\text{mA h g}^{-1}$ , respectively, at the rates of 0.5C, 1C, 2C and 5C. After 30 charge–discharge cycles, the capacities drop to 84.0, 68.8, 60.5 and 47.8  $\text{mA h g}^{-1}$ , respectively, with capacity retention of 64.6%, 64.3%, 75.3% and 78.8%. By comparison, the  $\text{Na}_2\text{MnSiO}_4/\text{C}$  composite (Fig. 6c and d) can only deliver 81.9, 59.2, 39.4 and 24.0  $\text{mA h g}^{-1}$  at the rates of 0.5C, 1C, 2C and 5C, respectively. After 30 charge–discharge cycles, the capacities decrease to 38.9, 32.7, 29.7 and 19.2  $\text{mA h g}^{-1}$ , respectively, with capacity retention of 47.5%, 55.3%, 73.3% and 76.6%. Furthermore, similar to  $\text{Li}_2\text{MnSiO}_4$  in Li ion cells, both  $\text{Na}_2\text{MnSiO}_4/\text{C}/\text{G}$  and  $\text{Na}_2\text{MnSiO}_4/\text{C}$  composites have different degrees of capacity fading with the increase of cycles. We assume that is related to the manganese dissolution and the Jahn–Teller effect of  $\text{Mn}^{3+}$  ions during the

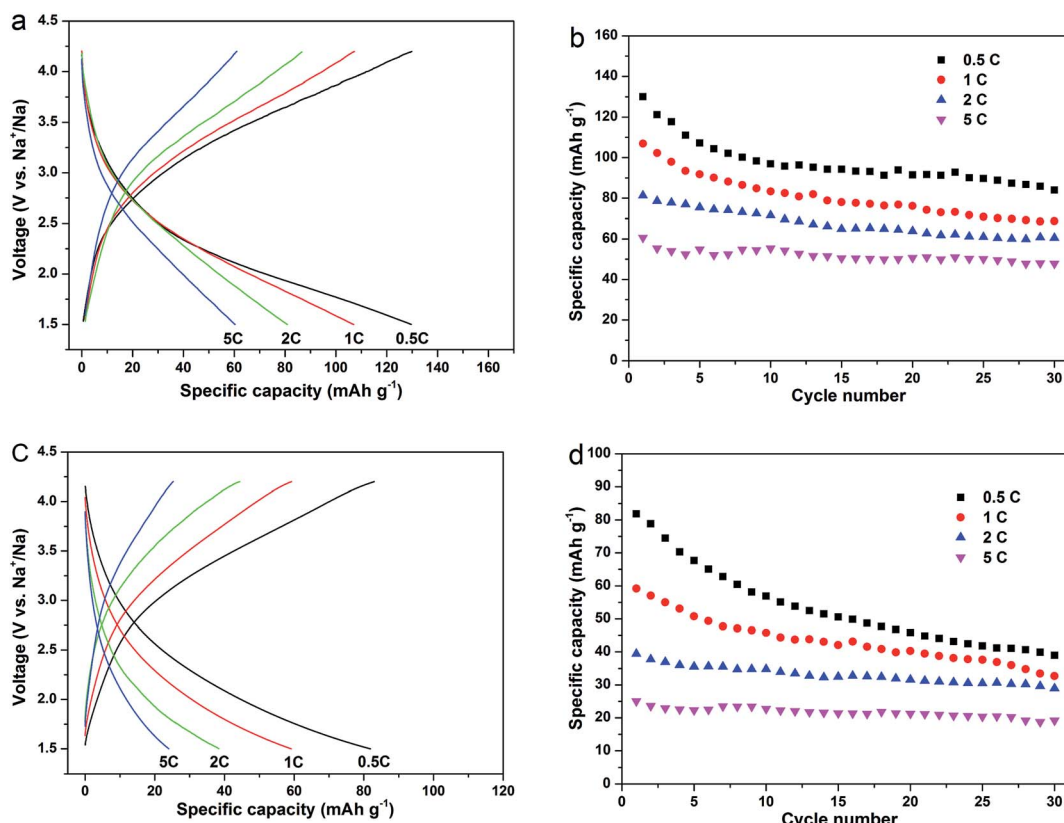


Fig. 6 The galvanostatic charge–discharge curves and the corresponding cyclabilities at rates of 0.5C, 1C, 2C and 5C for the composites ( $\text{Na}_2\text{MnSiO}_4/\text{C}/\text{G}$ : (a) and (b);  $\text{Na}_2\text{MnSiO}_4/\text{C}$ : (c) and (d)).

$\text{Na}^+$  insertion–extraction process, which can result in destruction of the active material structure.

In current literature, only few papers have reported the performances of the  $\text{Na}_2\text{MnSiO}_4$  as a cathode material for sodium ion batteries. Chen *et al.*<sup>20</sup> synthesized  $\text{Na}_2\text{MnSiO}_4/\text{C}$  by a sol–gel method and tested the electrochemical performances at different temperatures. At the rate of 0.1C, the reversible capacities of 70, 94 and 125  $\text{mA h g}^{-1}$  were obtained for the cell that was tested at 298, 323 and 363 K, respectively. Even at 363 K, the electrode only delivered capacities of 115, 76 and 55  $\text{mA h g}^{-1}$  at 1C, 3C and 5C, respectively, which are still lower than that of the  $\text{Na}_2\text{MnSiO}_4/\text{C}/\text{G}$  composite. In our work, the excellent electrochemical performances could be ascribed to the high conductivity and high specific surface area of graphene nanosheets, efficiently facilitating the electron transport and  $\text{Na}^+$  ion diffusion during the charge–discharge process, hence realizing the enhancements in rate and cycling performance of the active materials.

In order to further understand the kinetic characteristic of the  $\text{Na}_2\text{MnSiO}_4/\text{C}/\text{G}$  and  $\text{Na}_2\text{MnSiO}_4/\text{C}$  composites, the  $\text{Na}^+$  ion migration dynamics of the two composites were investigated from the electrochemical impedance spectroscopy (EIS) measurements. Fig. 7a exhibits the Nyquist curves of the composites after the third cycle at a rate of 0.1C at room temperatures. Both the composites show typical Nyquist plots with a depressed semicircle in the high–medium frequency region and a straight line at the low frequency region. An intercept along the real axis ( $Z_{\text{re}}$ ) at the highest frequency should be due to the internal resistance ( $R_{\text{e}}$ ) of the cell generating from the electrolyte, current collector, separator, *etc.*<sup>31,32</sup> The depressed semicircle in the middle frequency region is related to the charge-transfer resistance ( $R_{\text{ct}}$ ) through the solid–electrolyte interfaces. The linear plots in the low frequency region is attributed to Warburg impedance, which indicates the sodium ion diffusion in the solid phase. Meanwhile, the Nyquist plots are fitted using the equivalent circuit model, as shown in the insets of Fig. 7a. As can be seen, the  $R_{\text{ct}}$  of the  $\text{Na}_2\text{MnSiO}_4/\text{C}/\text{G}$  composite is 629.6 ohm which is much lower than that of the  $\text{Na}_2\text{MnSiO}_4/\text{C}$  composite (780.5 ohm), indicating that the electronic conductivity of the  $\text{Na}_2\text{MnSiO}_4/\text{C}/\text{G}$

**Table 1** Impedance parameters of the  $\text{Na}_2\text{MnSiO}_4/\text{C}/\text{G}$  and  $\text{Na}_2\text{MnSiO}_4/\text{C}$  composites

| Samples                                       | $R_{\text{e}}$ (Ω) | $R_{\text{ct}}$ (Ω) | $\sigma$ (Ω $\text{cm}^2 \text{s}^{-1/2}$ ) | $D_{\text{Na}^+}$ ( $\text{cm}^2 \text{s}^{-1}$ ) |
|---|--------------------|---------------------|---|---|
| $\text{Na}_2\text{MnSiO}_4/\text{C}/\text{G}$ | 5.2                | 629.6               | 89.3  | $9.17 \times 10^{-15}$                            |
| $\text{Na}_2\text{MnSiO}_4/\text{C}$          | 8.3                | 780.5               | 286.4                                       | $8.91 \times 10^{-16}$                            |

was dramatically improved after surface modification by graphene. Fig. 7b displays the curve of the relationship between  $Z_{\text{re}}$  and the reciprocal square root of frequency ( $\omega^{-1/2}$ ) in the low frequency region. The slope of the fitting line is the Warburg coefficient  $\sigma$ , it can be derived from eqn (1):<sup>33</sup>

$$Z_{\text{re}} = R_{\text{e}} + R_{\text{ct}} + \sigma\omega^{-1/2} \quad (1)$$

Therefore, according to the resulting  $\sigma$ , the sodium ion diffusion coefficient ( $D_{\text{Na}^+}$ ) could be obtained by the following eqn (2):<sup>33</sup>

$$D = R^2 T^2 / 2A^2 n^4 F^4 C^2 \sigma^2 \quad (2)$$

where  $R$  is the gas constant,  $T$  is the absolute temperature,  $A$  is the surface area of the cathode,  $n$  is the number of electrons transferred per molecule of  $\text{Na}_2\text{MnSiO}_4$ ,  $F$  is the Faraday constant,  $C$  is the concentration of sodium ion. Table 1 presents all the parameters obtained and the calculated sodium ion diffusion coefficient for the  $\text{Na}_2\text{MnSiO}_4/\text{C}/\text{G}$  and  $\text{Na}_2\text{MnSiO}_4/\text{C}$  composites. As shown, the calculated diffusion coefficients of sodium ions ( $D_{\text{Na}^+}$ ) are  $9.17 \times 10^{-15}$  and  $8.91 \times 10^{-16} \text{ cm}^2 \text{s}^{-1}$  for the  $\text{Na}_2\text{MnSiO}_4/\text{C}/\text{G}$  and  $\text{Na}_2\text{MnSiO}_4/\text{C}$  composites, respectively. The results of the EIS data well explains that the conductive graphene nanosheets could enhance the electronic conductivity and  $\text{Na}^+$  ion conductivity, and result in excellent charge–discharge performance.

Compared with  $\text{Na}_2\text{MnSiO}_4/\text{C}$ , the highly discharge capacity, good capacity retention, and enhanced rate capacity of  $\text{Na}_2\text{MnSiO}_4/\text{C}/\text{G}$  can be explained in the following aspects. On the one hand, the good electrical conductivity of graphene sheets

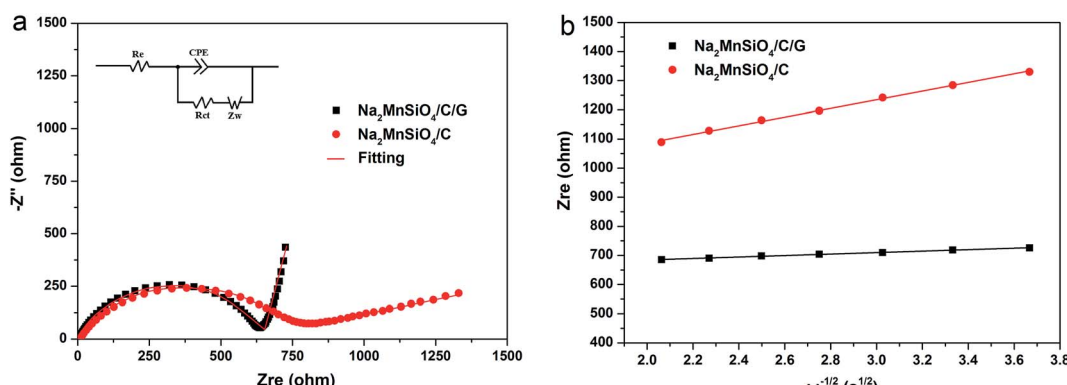


**Fig. 7** The Nyquist plots and equivalent circuit of composites  $\text{Na}_2\text{MnSiO}_4/\text{C}/\text{G}$  and  $\text{Na}_2\text{MnSiO}_4/\text{C}$  at room temperature (a) and the relationship between  $Z_{\text{re}}$  and  $\omega^{-1/2}$  in the low frequency region (b).



serve as continuous conductive channels between the  $\text{Na}_2\text{MnSiO}_4$  particles and the electrolyte. On the other hand, the adding of graphene oxide in the synthesis process could decrease the particles sizes of  $\text{Na}_2\text{MnSiO}_4$  and prevent the aggregation of nanoparticles, the homogeneous dispersion and nanoscale size of particles can increase the contact area of the active material and the electrolyte, which is benefited to the migration of sodium ions. In addition, the graphene sheets and the coating carbon in the composite can protect  $\text{Na}_2\text{MnSiO}_4$  from corrosive reactions with the electrolyte during the  $\text{Na}^+$  insertion/extraction process.

## 4. Conclusions

In conclusion, we have successfully synthesized  $\text{Na}_2\text{MnSiO}_4/\text{C}/\text{G}$  composite by assisted sol-gel method, in which  $\text{Na}_2\text{MnSiO}_4/\text{C}$  nanoparticles are homogeneously wrapped up in conductive and interconnected graphene nanosheets. Compared with a composite without graphene,  $\text{Na}_2\text{MnSiO}_4/\text{C}/\text{G}$  shows excellent electrochemical performances as the cathode material for sodium ion batteries. When evaluated in the sodium ion batteries configuration in the voltage range of 1.5–4.2 V (vs.  $\text{Na}^+/\text{Na}$ ) at room temperature, the  $\text{Na}_2\text{MnSiO}_4/\text{C}/\text{G}$  showed discharge capacities of 182.4, 130.1, 106.9, 80.3 and 60.7 mA h  $\text{g}^{-1}$  at the rates of 0.1C, 0.5C, 1C, 2C, 5C, respectively. For the cycling performances, the capacity retentions of the composite can still maintain at 64.3%, 75.3% and 78.8% at the rates of 1C, 2C, and 5C after 30 cycles, respectively. The superior electrochemical performance of  $\text{Na}_2\text{MnSiO}_4/\text{C}/\text{G}$  composite might originate from the conductive graphene nanosheets and nanoscale size  $\text{Na}_2\text{MnSiO}_4$  particles. It is interesting to note that the sodium ion insertion–extraction process of  $\text{Na}_2\text{MnSiO}_4$  is similar to that of  $\text{Li}_2\text{MnSiO}_4$  as cathode in Li ion batteries, despite the capacities observed and the corresponding energy densities are lower. In future, though further study,  $\text{Na}_2\text{MnSiO}_4$  will become very competitive candidates as the cathodes for Na ion batteries.

## Acknowledgements

This study was the financially supported by Science and Technology Research Project of Education Department of Hubei Province (Q20162804) and Start up Foundation of Hubei University of Science and Technology (BK1519).

## Notes and references

- 1 J. M. Tarascon and M. Armand, *Nature*, 2001, **414**, 359–367.
- 2 H. Pan, Y. S. Hu and L. Q. Chen, *Energy Environ. Sci.*, 2013, **6**, 2338–2360.
- 3 M. Armand and J. M. Tarascon, *Nature*, 2008, **451**, 652–657.
- 4 J. B. Goodenough and Y. Kim, *Chem. Mater.*, 2010, **22**, 587–603.
- 5 V. Palomares, P. Serras, I. Villaluenga, K. B. Hueso, J. Carretero-Gonzalez and T. Rojo, *Energy Environ. Sci.*, 2012, **5**, 5884–5901.
- 6 Y. Cao, L. Xiao, W. Wang, D. Choi, Z. Nie, J. Yu, L. V. Saraf, Z. Yang and J. Liu, *Adv. Mater.*, 2011, **23**, 3155–3160.
- 7 H. Kim, Z. Ding, M. H. Lee, K. Lim, G. Yoon and K. Kang, *Adv. Energy Mater.*, 2016, **6**, 1600943–1600981.
- 8 C. Delmas, J. J. Braconnier, C. Fouassier and P. Hagenmuller, *Solid State Ionics*, 1981, **3–4**, 165–169.
- 9 M. D'Arienzo, R. Ruffo, R. Scotti, F. Morazzoni, C. M. Maria and S. Polizzi, *Phys. Chem. Chem. Phys.*, 2012, **14**, 5945–5952.
- 10 A. Caballero, L. Hernan, J. Morales, L. Sanchez, J. S. Pena and M. A. G. Aranda, *J. Mater. Chem.*, 2002, **12**, 1142–1147.
- 11 F. Sauvage, L. Laffont, J. M. Tarascon and E. Baudrin, *Inorg. Chem.*, 2007, **46**, 3289–3294.
- 12 J. Zhao, L. Zhao, N. Dimov, S. Okada and T. Nishida, *J. Electrochem. Soc.*, 2013, **160**, A3077–A3081.
- 13 D. Carlier, J. H. Cheng, R. Berthelot, M. Guignard, M. Yoncheva, R. Stoyanova, B. J. Hwang and C. Delmas, *Dalton Trans.*, 2011, **40**, 9306–9312.
- 14 R. Klee, M. J. Aragón, P. Lavela, R. Alcántara and J. L. Tirado, *ACS Appl. Mater. Interfaces*, 2016, **35**, 23151–23159.
- 15 H. Li, C. Wu, Y. Bai, F. Wu and M. Wang, *J. Power Sources*, 2016, **326**, 14–22.
- 16 W. Tang, X. Song, Y. Du, C. Peng, M. Lin, Y. P. Wu, F. Pan and K. P. Loh, *J. Mater. Chem. A*, 2016, **4**, 4882–4892.
- 17 P. Barpanda, G. Oyama, S. Nishimura, S. C. Chung and A. Yamada, *Nat. Commun.*, 2014, **5**, 4358–4366.
- 18 A. Caballero, L. Hernan, J. Morales, L. Sanchez, J. S. Pena and M. A. G. Aranda, *J. Mater. Chem.*, 2002, **12**, 1142–1147.
- 19 Y. X. Zhang, H. J. Yu and H. S. Zhou, *J. Mater. Chem. A*, 2014, **2**, 11574–11577.
- 20 C. Y. Chen, K. Matsumoto, T. Nohira and R. Hagiwara, *Electrochim. Commun.*, 2014, **45**, 63–66.
- 21 W. S. Hummers and R. E. Offeman, *J. Am. Chem. Soc.*, 1958, **80**, 1339.
- 22 H. Duncan, A. Kondamreddy, P. H. J. Mercier, Y. Le Page, Y. Abu-Lebdeh, M. Couillard, P. S. Whitfield and I. J. Davidson, *Chem. Mater.*, 2011, **23**, 5446–5456.
- 23 F. Bonhomme, J. C. Lassegues and L. Servant, *J. Electrochem. Soc.*, 2001, **148**, 450–458.
- 24 H. Zhu, H. B. He, X. L. Ma, L. Zan and Y. X. Zhang, *Electrochim. Acta*, 2015, **115**, 116–124.
- 25 H. L. Wang, J. T. Robinson, G. Diankov and H. J. Dai, *J. Am. Chem. Soc.*, 2010, **132**, 3270–3271.
- 26 S. Devaraj, M. Kuezma, C. T. Ng and P. Balaya, *Electrochim. Acta*, 2013, **102**, 290–298.
- 27 H. X. Gong, Y. C. Zhu, L. L. Wang, D. H. Wei, J. W. Liang and Y. T. Qian, *J. Power Sources*, 2014, **246**, 192–197.
- 28 A. Kokalj, R. Dominko, G. Mali, A. Meden, M. Gaberscek and J. Jamnik, *Chem. Mater.*, 2007, **19**, 3633–3640.
- 29 R. Dominko, M. Bele, A. Kokalj, M. Gaberscek and J. Jamnik, *J. Power Sources*, 2007, **174**, 457–461.
- 30 R. Dominko, *J. Power Sources*, 2008, **184**, 462–468.
- 31 S. K. Liu, J. Xu, D. Z. Li, Y. Hu, X. Liu and K. Xie, *J. Power Sources*, 2013, **232**, 258–263.
- 32 H. Qiu, K. Zhu, H. Li, T. Li, T. Zhang, H. Yue, Y. Wei, F. Du, C. Wang, G. Chen and D. Zhang, *Carbon*, 2015, **87**, 365–373.
- 33 A. J. Bard and J. R. Faulkner, *Electrochemical methods*, Wiley, 2nd edn, 2001, p. 231.

